

Article

Development and Mechanistic Studies of Ternary Nanocomposites for Hydrogen Production from Water Splitting to Yield Sustainable/Green Energy and Environmental Remediation

Asim Jilani ^{1,*}, Syed Zajif Hussain ², Ammar A. Melaibari ^{1,3} and Nidal H. Abu-Hamdeh ^{3,4}¹ Center of Nanotechnology, King Abdulaziz University, Jeddah 21589, Saudi Arabia; aamelaibari@kau.edu.sa² Department of Chemistry & Chemical Engineering, SBA-School of Science & Engineering (SBA-SSE), Lahore University of Management Sciences (LUMS), Lahore 54792, Pakistan; syed.hussain@lums.edu.pk³ Department of Mechanical Engineering, King Abdulaziz University, Jeddah 21589, Saudi Arabia; nabuhamdeh@kau.edu.sa⁴ Center of Research Excellence in Renewable Energy and Power System, King Abdulaziz University, Jeddah 21589, Saudi Arabia

* Correspondence: asim.jilani@gmail.com or ajilani@kau.edu.sa; Tel.: +966-599693297

Abstract: Photocatalysts lead vitally to water purifications and decarbonise environment each by wastewater treatment and hydrogen (H₂) production as a renewable energy source from water-photolysis. This work deals with the photocatalytic degradation of ciprofloxacin (CIP) and H₂ production by novel silver-nanoparticle (AgNPs) based ternary-nanocomposites of thiolated reduce-graphene oxide graphitic carbon nitride (AgNPs-S-rGO_{2%}@g-C₃N₄) material. Herein, the optimised balanced ratio of thiolated reduce-graphene oxide in prepared ternary-nanocomposites played matchlessly to enhance activity by increasing the charge carriers' movements via slowing down charge-recombination ratios. Reduced graphene oxide (rGO), >2 wt.% or <2 wt.%, rendered H₂ production by light-shielding effect. As a result, CIP degradation was enhanced to 95.90% by AgNPs-S-rGO_{2%}@g-C₃N₄ under the optimised pH(6) and catalyst dosage(25 mg/L) irradiating beneath visible-light (450 nm, 150 watts) for 70 min. The chemical and morphological analysis of AgNPs-S-rGO_{2%}@g-C₃N₄ surface also supported the possible role of thiolation for this enhancement, assisted by surface plasmon resonance of AgNPs having size < 10 nm. Therefore, AgNPs-S-rGO_{2%}@g-C₃N₄ has 3772.5 μmol⁻¹ h⁻¹ H₂ production, which is 6.43-fold higher than g-C₃N₄ having cyclic stability of 96% even after four consecutive cycles. The proposed mechanism for AgNPs-S-rGO_{2%}@g-C₃N₄ revealed that the photo-excited electrons in the conduction-band of g-C₃N₄ react with the adhered water moieties to generate H₂.

Keywords: water treatment; photocatalytic hydrogen production; nanocomposites; antibiotic; photocatalytic degradation



Citation: Jilani, A.; Hussain, S.Z.; Melaibari, A.A.; Abu-Hamdeh, N.H. Development and Mechanistic Studies of Ternary Nanocomposites for Hydrogen Production from Water Splitting to Yield Sustainable/Green Energy and Environmental Remediation. *Polymers* **2022**, *14*, 1290. <https://doi.org/10.3390/polym14071290>

Academic Editor: Wael Mamdouh

Received: 27 December 2021

Accepted: 17 March 2022

Published: 23 March 2022

Publisher's Note: MDPI stays neutral with regard to jurisdictional claims in published maps and institutional affiliations.



Copyright: © 2022 by the authors. Licensee MDPI, Basel, Switzerland. This article is an open access article distributed under the terms and conditions of the Creative Commons Attribution (CC BY) license (<https://creativecommons.org/licenses/by/4.0/>).

1. Introduction

Hydrogen (H₂) production through the photolysis of water is an alternative renewable green energy source with the prime advantages of harvesting energy and eco-friendly nature. The splitting of water under solar radiation or a light source of suitable wavelength is pertinent to the advent of new photocatalysts [1,2]. For this, various nanostructured semiconducting materials have been explored, such as titanium dioxide (TiO₂), (g-C₃N₄), cadmium sulphide (CdS), zinc oxide (ZnO) and cerium(IV) [3]. However, the efficiency of single semiconductor photocatalysts is low due to the absorption of light in a small range of spectrum and the poor charge separation abilities leading to a high rate of electron-hole pair recombination. These problems have been addressed by engineering the appropriate bandgap and improving charge-recombination ratios or electron affinities for a radiation

source using a combination of semiconducting materials with conducting oxides of metals or non-metals [4,5]. This combination develops the heterojunctions at recombinants' interfaces and results in band-bending to charge separations by forcing their photogenerated charge carriers to move in reverse directions [6,7]. Therefore, by using the combination of binary or tertiary nanocomposite-based photocatalysts, the maximum H₂ production can be obtained from water under certain experimental conditions by overcoming the listed issues [8].

Ciprofloxacin (CIP) is a broad-spectrum antibiotic with low-biodegradability being discharged at high volumes ranging from µg/L to mg/L into wastewaters of hospitals and pharmaceutical industries [9]. Its rise into water bodies poses a significant threat to the environment by increasing drug resistance in bacteria. Its elimination from the environment thus requires an urgent and efficient means. Accordingly, different techniques such as physical adsorption onto various substrates and biological, electrochemical, and photocatalytic degradations have been reported [10]. Among these, the photocatalytic approach has been most distinguished in eliminating the CIP pollutants due to high effectivity and ecological sustainability. The charge-carriers such as electron and hole (e⁻ and h⁺) pairs produced by these photocatalysts, all under the influence of light-irradiation, are the source to generate the reactive-oxygen species such as hydroxyl and superoxide ([•]OH and O₂⁻) radicals, responsible for the degradation of CIP molecules. It has been observed that the degradation of CIP molecules has been enhanced using heterojunctions or composites of semiconducting materials with metal nanoparticles [11]. The doping of sulphur (S) in *g*-C₃N₄ and rGO helped us modify their electrical conductivity and bandgap required for photodegradation of CIP molecules. This doping of S into these semiconductors further supports forming the smaller sized AgNPs. It results from changes in their pristine optical absorptions by activating these photocatalysts under higher visible ranges.

Among the previously mentioned photocatalysts, *g*-C₃N₄ has attained the scientific community's attention for photocatalytic H₂ production. The popularity of *g*-C₃N₄ is attributed to its non-toxicity, ease of synthesis, and tuneable nature of its bandgap [12]. Furthermore, its physio-chemical stability is due to covalent bonding between nitrogen and carbon, allowing it to function equally well in acidic and basic media. Additionally, the negative band potential of *g*-C₃N₄ (around 1.3 eV) facilitates photocatalytic H₂ production and water oxidation reaction under visible light [13]. However, the competence of pure *g*-C₃N₄ for photocatalytic H₂ production is far less due to rapid charge-recombination ratios and the existence of a wide bandgap (of around 2.7 eV). Therefore, doping of *g*-C₃N₄ with other materials such as cadmium sulphide, molybdenum disulphide, gold, graphene and low dimension carbon-based materials supports the suppression of rapid charge recombinations and narrows the bandgap, which is highly required for large-scale photocatalytic H₂ production [14,15]. Among these materials, reduced graphene oxide (rGO) seems a promising co-catalyst due to its conjugated structure, high specific surface area, and the tuneable nature of electronic bands [16].

Notably, the proportion of rGO as co-catalyst in the composite catalyst is crucial for photocatalytic H₂ production and energy application [17]. The higher amount of rGO produces negative shielding effects [18], which slow down the charge carriers' movement from the valence band (VB) to the conduction band (CB), ultimately affecting the H₂ production. Consequently, the efficiency of rGO@*g*-C₃N₄ can be further enhanced after adjusting the amount of rGO in *g*-C₃N₄ to a specific ratio. Additionally, doping with elements with low electronegativities, such as boron (B) and sulphur (S), can also boost the catalytic efficiency by raising the Fermi level [19]. Thus, the thiolation of composite materials, rGO and *g*-C₃N₄, can enhance photocatalytic H₂ production in two ways, by dropping the charge-recombination ratios and increasing the light absorption adeptness. The thiolation help to conquer the negative shielding effect of thiolated rGO (HS-rGO), increasing its absorption efficiency and the increased carbon vacancies in thiolated *g*-C₃N₄ (HS-*g*-C₃N₄) act as active territories to reduce the chance of charge recombinations [20]. In summary, thiolation increases the charge separation capabilities of both HS-rGO and HS-*g*-C₃N₄. Interestingly, photocatalytic H₂ production can be further improved by coupling

thiolated composites with some noble metal nanoparticles (NPs), such as silver. The silver nanoparticles (AgNPs) are highly conductive and support photocatalysis for H₂ production through surface plasmon resonance (SPR). This SPR property also assists the movement of charge carriers, enhancing photocatalytic H₂ production [21,22].

A literature review showed that various groups had synthesised rGO and its composites with g-C₃N₄ at a fixed amount of rGO for photocatalytic hydrogen production. In this context, Jaiswal et al. prepared the rGO-based composites of g-C₃N₄ using a constant 5 wt.% [23]. Likewise, Ibrahim and his colleagues investigated the TiO₂/rGO/g-C₃N₄ system for H₂ production with a fixed 1 wt.% of rGO [24]. In the same way, Pan et al. [25] explored the effect of 0.3% rGO in their rGO@g-C₃N₄ composites for hydrogen production. However, the impact of thiolation has not been analysed, and the concentration of thiolated rGO (HS-rGO) in ternary-nanocomposites for H₂ production can be further optimised.

In view of the previous reports [12,19,20,23–25], rGO-based composites of g-C₃N₄ were prepared at different concentrations of HS-rGO, from 1 to 4 wt.%. The thiolated composite (HS-rGO@g-C₃N₄) with an optimised concentration of HS-rGO of 2 wt.% was selected based on photoluminescence (PL) studies which indicated lesser charge recombinations. HS-rGO_{2%}@g-C₃N₄ was found to have improved structural and chemical properties and is highly desirable for photocatalytic H₂ production. Next, the HS-rGO_{2%}@g-C₃N₄ was decorated with AgNPs to produce AgNPs-S-rGO_{2%}@g-C₃N₄. The charge transfer, structural, surface chemical, optical conduction, and photocatalytic H₂ production properties of this final nanocomposite, AgNPs-S-rGO_{2%}@g-C₃N₄, were explored under the same experimental conditions compared to HS-rGO_{2%}@g-C₃N₄ and rGO_{2%}@g-C₃N₄.

2. Experimental Details

2.1. Synthesis and Thiolation of rGO

Sheets of graphene oxide (GO) were synthesised using a modified Hummer method as per our previous work [26]. After this, GO sheets were heated to 200 °C for 2 h to obtain rGO. This rGO was thiolated following an earlier report with minor modifications [27]: 50 mg of rGO was dispersed in 50 mL of ultrapure deionised-water and ultrasonicated for 1.5 h, followed by the addition of 3 mL of HBr and further sonication for 2 h. After this, 2.5 g of thiocarbamide was added at 80 °C and stirred continuously for 24 h. The reaction was stopped, and the reaction media was allowed to cool to room temperature. Afterwards, 25 mL of 4 M aqueous solution of KOH was added and stirred for a further 1 h. The black suspension of thiolated GO (HS-rGO) was filtrated through a PTFE membrane filter (0.2 µm) and washed many times with dimethyl ether, ethanol, and water. The resulting HS-rGO nanosheets were redispersed into ultrapure water by sonication and vacuum dried before further use.

2.2. Synthesis of Graphitic Carbon Nitride Nanosheets (g-C₃N₄)

To prepare g-C₃N₄, a pale-yellow powder, 2.5 g of melamine was heated in the muffle-furnace to 525 °C by providing 10 °C min⁻¹ heating rate as per previous reports by Zhang et al. [28].

2.3. Synthesis of Thiolated Graphitic Carbon Nitride Nanosheets (HS-g-C₃N₄)

HS-g-C₃N₄ was prepared by following the Wang's protocol via the single-step thermal-polymerisation of thiocarbamide [13]. For this, 30 g of thiocarbamide was kept in a porcelain crucible with no lid. This open crucible was placed into another large crucible bolted with a lid and placed to heat in a muffle-furnace to 550 °C for 5 h by providing a temperate rate of 2 °C min⁻¹. This process resulted in a pale-yellow coloured powder, HS-g-C₃N₄, which accumulated in the larger crucible.

2.4. Fabrication of rGO@g-C₃N₄ and HS-rGO@g-C₃N₄

To fabricate rGO@g-C₃N₄ with different concentrations of rGO, 4.7 g of g-C₃N₄ was added separately into 15 mL solution of rGO prepared using 1, 2, 3 and 4 wt.% rGO

according to the measured mass of $g\text{-C}_3\text{N}_4$. These four mixtures were then vigorously sonicated under slow stirring for 1 h to coat rGO onto the $g\text{-C}_3\text{N}_4$. Next, the rGO-coated $g\text{-C}_3\text{N}_4$ ($\text{rGO}@g\text{-C}_3\text{N}_4$) was filtered from the solution and vacuum dried. The $\text{rGO}@g\text{-C}_3\text{N}_4$ with 2 wt.% of rGO ($\text{rGO}_{2\%}@g\text{-C}_3\text{N}_4$) was found best, as illustrated by the PL study. Further, the same composite was prepared using 2 wt.% of HS-rGO to HS- $g\text{-C}_3\text{N}_4$ ($\text{HS-rGO}_{2\%}@g\text{-C}_3\text{N}_4$). Finally, the HS- $\text{rGO}_{2\%}@g\text{-C}_3\text{N}_4$ was decorated with AgNPs to make the ternary composites.

2.5. Synthesis of AgNPs onto the Surface of HS- $\text{rGO}_{2\%}@g\text{-C}_3\text{N}_4$

AgNPs were prepared over HS- $\text{rGO}_{2\%}@g\text{-C}_3\text{N}_4$ nanosheets via the reduction of silver ions. In this context, 45 mg of HS- $\text{rGO}_{2\%}@g\text{-C}_3\text{N}_4$ nanosheets were mixed into 50 mL (2 mM) of AgNO_3 solution in a round bottom flask fixed in an ice bath under continuous stirring. Under these conditions, this mixture was sonicated for 30 min to obtain a uniform distribution. Then 20 mL (25 mM) of NaBH_4 solution was added dropwise to reduce the silver ions in the prepared dispersion to prepare the AgNPs and attach them to the thiol positions on the nanosheets to yield AgNP-decorated HS- $\text{rGO}_{2\%}@g\text{-C}_3\text{N}_4$ ($\text{AgNPs-S-rGO}_{2\%}@g\text{-C}_3\text{N}_4$). Finally, the prepared AgNPs-S- $\text{rGO}_{2\%}@g\text{-C}_3\text{N}_4$ nanosheets were washed several times with deionised water and methanol by centrifuging them at 8000 rpm, and vacuum dried before further use. The synthetic scheme of $\text{AgNPs-S-rGO}_{2\%}@g\text{-C}_3\text{N}_4$ (Figure 1).

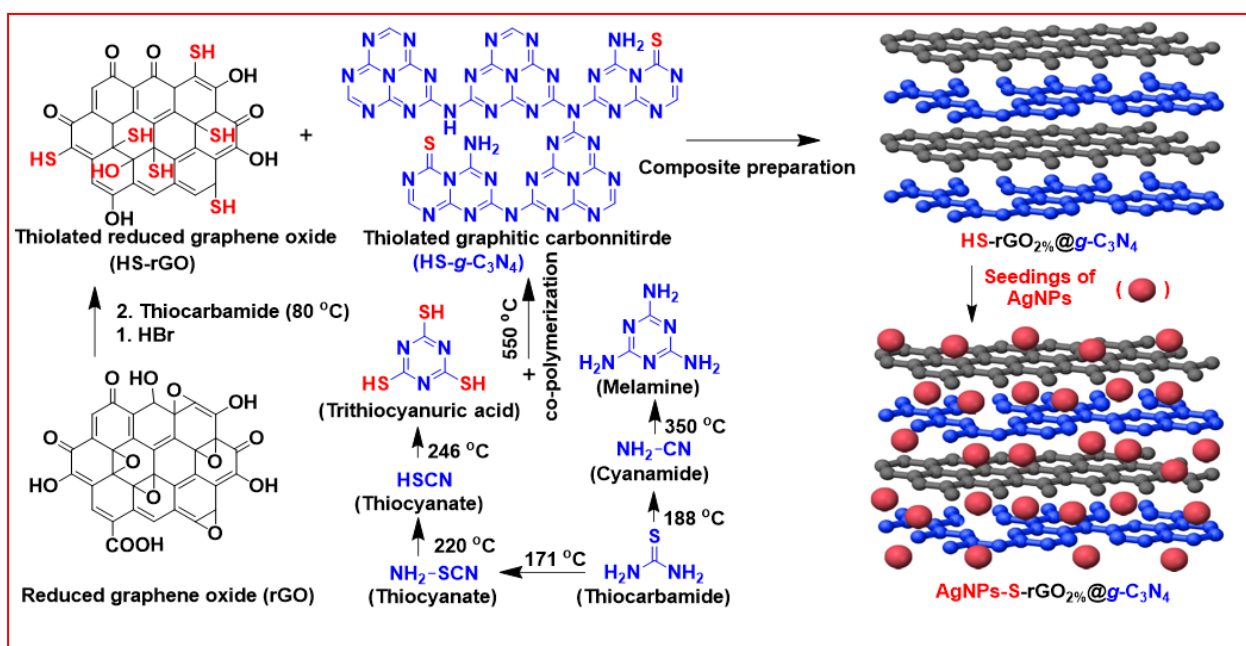


Figure 1. Scheme for the synthesis of $\text{AgNPs-S-rGO}_{2\%}@g\text{-C}_3\text{N}_4$.

2.6. Characterisations

Structural properties of $g\text{-C}_3\text{N}_4$, HS- $\text{rGO}@g\text{-C}_3\text{N}_4$ and $\text{AgNPs-S-rGO}@g\text{-C}_3\text{N}_4$ were studied between diffraction angles from 5 to 80° using X-ray diffraction (XRD), Rigaku Ultima-IV Tokyo Japan. The optical properties were explored using photoluminescence spectroscopy (PL-Kimon 1.K) and UV-Visible diffuse reflectance spectroscopy (HACH LANGE DR 6000). Surface and functional analysis were performed by X-ray photoelectron spectroscopy (PHI-VersaProbII, PHI, Chanhassen, MN, USA) under a high vacuum (10^{-7} Pa). Morphology and chemical nature of these samples were explored using a Nova NanoSEM 450 (FEI, Hillsboro, OR, USA) equipped with an Everhart-Thornley detector (ETD), a scanning transmission electron detector (STEM), and an energy dispersive X-ray detector (EDX), operated between 15 to 25 kV at a working distance of 5 mm. The evolution of H_2 was scrutinised using gas chromatography (Agilent Technologies 7890B-GC System, Santa Clara, CA, USA).

2.7. Hydrogen Production

The photocatalytic study was conducted in a Pyrex beaker that contained 15 mg of AgNPs-S-rGO_{2%}@g-C₃N₄. The same sacrificial reagent (15% triethanolamine) was used in all experiments. However, before starting the photocatalytic generation of H₂, surface-adsorbed oxygen moieties were removed by degassing this reaction assembly with sustained nitrogen gas flow for 1 h. These experiments have been performed under visible light (150 Watt, Xe lamp). The evolution of H₂ was scrutinised at regular intervals of 30 min, using gas chromatography (Agilent Technologies, 7890B-GC System). Furthermore, AgNPs-S-rGO_{2%}@g-C₃N₄ was tested for reusability under the same experimental conditions by four times repeating the experiment.

2.8. Photocatalytic Degradation of Ciprofloxacin Antibiotics

A Ciprofloxacin antibiotic (CIP) was chosen as a model pollutant for the photocatalytic ability of AgNPs-S-rGO_{2%}@g-C₃N₄. Therefore, 25 mg/L concentration of CIP was prepared. The photocatalytic degradation of CIP was investigated under visible light (450 nm, 150 watts, distance from light source to CIP solution 40 cm, and light intensity 74.64 w/m²) at room temperature while maintaining pH 7 during the study. However, the solution was kept in the dark for 20 min before irradiating to achieve the absorption equilibrium. Afterwards, the CIP solution was started irradiating, and 3 mL was taken with the regular interval of 10 min to analyse the degradation of CIP. The following equation was used to calculate the degradation parameters of CIP [29].

$$\text{Degradation (\%)} = \left(\frac{C_0 - C}{C_0} \right) 100 \quad (1)$$

In the above equation, C_0 and C represents the initial and final concentration of CIP, respectively. Further, the following equation was used to calculate the kinetic rate constant (k) during photocatalytic degradation of CIP [30].

$$\ln \left(\frac{C}{C_0} \right) = -kt \quad (2)$$

3. Results and Discussion

3.1. Structural Analysis

The diffraction pattern of rGO_{2%}@g-C₃N₄ shown in Figure 2 indicated that the peaks that appear at around $2\theta = 13.26^\circ$ and 27.46° are attributed to the (001) and (002) diffraction planes, respectively, of the hexagonal form of g-C₃N₄ (JCPDS # 01-087-1526) [31]. The diffraction plane (001) is associated with in-plane structural packing of tri-s-triazine with an interlayer spacing of 0.66 nm.

In comparison, (002) is related to interlayer aromatic stacking of C-N having the interlayer spacing of 0.32 nm [32]. However, the diffraction peaks of rGO could not be seen due to the reduction in functional moieties anchored with its basal plane. The absence of diffraction peaks for rGO is consistent with an earlier study [33]. Compared to rGO_{2%}@g-C₃N₄, the peak (001) in the diffraction patterns of HS-rGO_{2%}@g-C₃N₄ was shifted from $2\theta = 13.26^\circ$ to 12.99° , whereas (002) moved from $2\theta = 27.46^\circ$ to 27.5° . After thiolation, the shifting of the diffraction planes is attributed to incorporating the sulphur atoms into the copolymerised sheets of the g-C₃N₄ and within the layered assemblies of the rGO. This incorporation resulted in the reduction of the thickness of the layers in these composites [13]. In the case of AgNPs-S-rGO_{2%}@g-C₃N₄, additional diffraction peaks at around 38.18° and 44.36° were observed. These were, respectively, attributed to the (111) and (200) planes of silver, as per JCPDS # 00-001-1164. Moreover, in AgNPs-S-rGO_{2%}@g-C₃N₄, the small shifts of the (001) and (002) peaks towards lower diffraction angles are attributed to the successful interaction of AgNPs with HS-rGO_{2%}@g-C₃N₄. These shifts are associated with the covalent interactions of AgNPs with the thiol moieties of HS-rGO_{2%}@g-C₃N₄, which separates and keeps intact the layered assemblies of the composite material. This is due to the difference

in atomic radii of silver, carbon and nitrogen [34]. Ag has a higher atomic radius (0.144 nm) in comparison to carbon (0.077 nm) and nitrogen (0.075 nm) [34]. Therefore, this difference was valuable for promoting successful interaction, which further enhanced light harvesting, resulting in higher photocatalytic H₂ production.

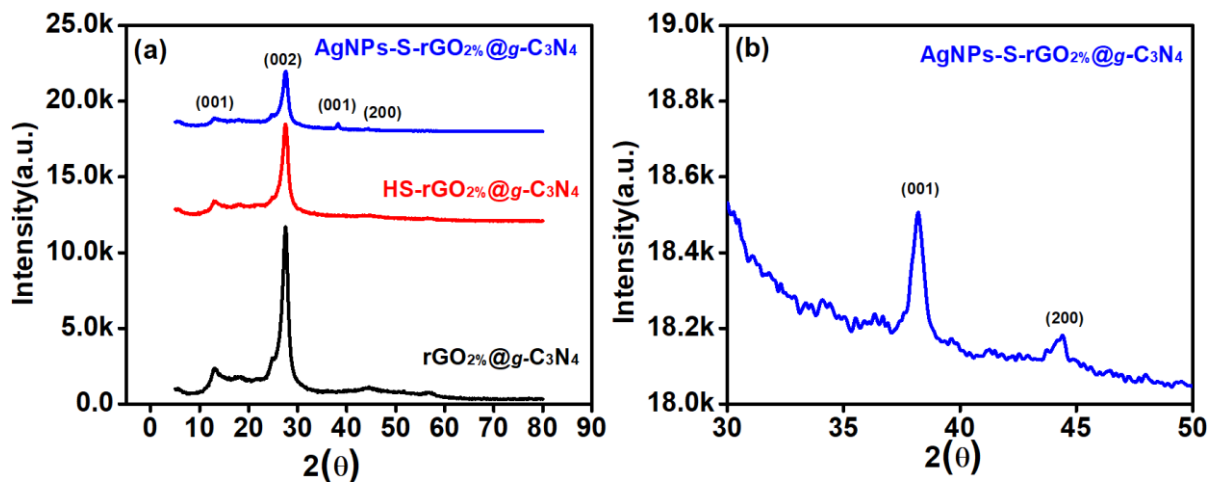


Figure 2. (a) Diffraction patterns of rGO_{2%}@g-C₃N₄, HS-rGO_{2%}@g-C₃N₄ and AgNPs-S-rGO_{2%}@g-C₃N₄ whilst (b) enlarged spectra of AgNPs-S-rGO_{2%}@g-C₃N₄ taken between 30 to 50°.

3.2. Optical Properties

The optical properties give insight into the charge transfer from the VB to the CB, directly impacting the material's ability to generate H₂ from the water splitting. Therefore, UV-Visible diffuse reflectance spectroscopy was employed to explore the charge transfer conduction rate of rGO_{2%}@g-C₃N₄, HS-rGO_{2%}@g-C₃N₄, and AgNPs-S-rGO_{2%}@g-C₃N₄. The absorption peaks of rGO_{2%}@g-C₃N₄ were shifted to a higher wavelength after thiolation (HS-rGO_{2%}@g-C₃N₄) and moved further following seeding with AgNPs (AgNPs-S-rGO_{2%}@g-C₃N₄), as shown in Figure 3a. Compared to rGO_{2%}@g-C₃N₄, an increase in the light absorption ability of HS-rGO_{2%}@g-C₃N₄ is attributed to thiolation [35]. The associated thiol moieties are excellent hole quenchers and are well known to reduce the recombination rates of electron-hole pairs in the resulting composites [20]. Further, in the case of AgNPs-S-rGO_{2%}@g-C₃N₄, the characteristic SPR of AgNPs enhances light absorption. However, the SPR is dependent on the size of the AgNPs. However, a non-observable SPR peak hump was noticed for AgNPs-S-rGO_{2%}@g-C₃N₄ caused by two possible reasons (Figure 3a). First, the interaction of thiolated rGO with AgNPs can lead to quenching the SPR in AgNPs-S-rGO_{2%}@g-C₃N₄ because of the difference in their dielectric constants [35]. A second possible reason may be low concentrations or average particle size (<10 nm). Thus, if the AgNPs have a size within a range of a few nanometres or the amount impregnated is low, their SPR will remain imperceptible [36]. In our case, the size of the AgNPs that could be seen in TEM analysis was found to be less than 10 nm, but their low concentration as determined by the XPS survey scan (Figure S2 and Table S1, Supplementary Materials) could be the second reason for the absence of the AgNPs SPR in the absorbance spectrum of AgNPs-S-rGO_{2%}@g-C₃N₄.

The change in the absorbance of light can further transform the conduction behaviour of the subjected material, which negatively affects hydrogen production. Therefore, the Kubelka–Munk function was used to estimate the conduction behaviour of rGO_{2%}@g-C₃N₄, HS-rGO_{2%}@g-C₃N₄ and AgNPs-S-rGO_{2%}@g-C₃N₄ (Figure 3b) [37]. The bandgap calculated for rGO_{2%}@g-C₃N₄ was 2.50 eV, which is less than that of g-C₃N₄ [38]. Further, reduction in bandgap value of g-C₃N₄ after the addition of rGO is ascribed to the interactions by covalent bonding between carbon atoms in g-C₃N₄ and rGO [39]. This interaction leads to the reduction of the bandgap for rGO_{2%}@g-C₃N₄. The bandgap of rGO_{2%}@g-C₃N₄ was further reduced after thiolation and was about 2.46 eV for HS-rGO_{2%}@g-C₃N₄. This

decrease in the bandgap after thiolation is attributed to the enhanced strong affinity between the functional groups of $g\text{-C}_3\text{N}_4$ and rGO, leading to improved absorption of light with enhanced charge transfer behaviour between their CB the VB [40]. Further, the bandgap was reduced to 2.42 eV $\text{AgNPs-S-rGO}_{2\%}@g\text{-C}_3\text{N}_4$. However, during this transfer, these charge carriers may recombine, which hinders H_2 production. Therefore, the charge recombination ratio of $\text{rGO}_{2\%}@g\text{-C}_3\text{N}_4$, $\text{HS-rGO}_{2\%}@g\text{-C}_3\text{N}_4$, and $\text{AgNPs-S-rGO}_{2\%}@g\text{-C}_3\text{N}_4$ was estimated using the PL spectra (Figure 3c). The intensity of the PL spectra is directly proportional to the ratio of charge recombinations. The PL spectra of pure $g\text{-C}_3\text{N}_4$ (Figure S1) showed strong emission, attributed to the rapid recombinations of charge carriers. However, the PL intensity was reduced with the addition of rGO to the $g\text{-C}_3\text{N}_4$. The addition of rGO to $g\text{-C}_3\text{N}_4$ behave as shuttle for excited electrons to move from $g\text{-C}_3\text{N}_4$ to rGO at the interface between them and it deters the charge recombination [41]. Therefore, the intensity of the PL spectra for $\text{rGO}_{1\%}@g\text{-C}_3\text{N}_4$ (Figure S1) was less than that of the pristine $g\text{-C}_3\text{N}_4$ and was further reduced for $\text{rGO}_{2\%}@g\text{-C}_3\text{N}_4$. However, as the percentage of rGO increased from 2 wt.% to 3 wt.% and 4 wt.% (Figure S1), the PL intensity increased, which indicates the rapid recombination of charged particles in $\text{rGO}_{3\%}@g\text{-C}_3\text{N}_4$ and $\text{rGO}_{4\%}@g\text{-C}_3\text{N}_4$. The increase in PL intensity at a higher percentage (above 2% in our case) is attributed to the negative shielding effect of rGO, which enhanced the charge-recombination ratios for $\text{rGO}_{3\%}@g\text{-C}_3\text{N}_4$ and $\text{rGO}_{4\%}@g\text{-C}_3\text{N}_4$ [42]. Therefore, we selected $\text{rGO}_{2\%}@g\text{-C}_3\text{N}_4$ for thiolation. The PL intensity of $\text{HS-rGO}_{2\%}@g\text{-C}_3\text{N}_4$ was reduced than that of $\text{rGO}_{2\%}@g\text{-C}_3\text{N}_4$ and was further reduced (Figure 3c) after adding AgNPs. The reduction of the PL intensity after thiolation and seeding with AgNPs ($\text{AgNPs-S-rGO}_{2\%}@g\text{-C}_3\text{N}_4$) showed that the charge recombination ratio has reduced to the point desired for enhanced H_2 production.

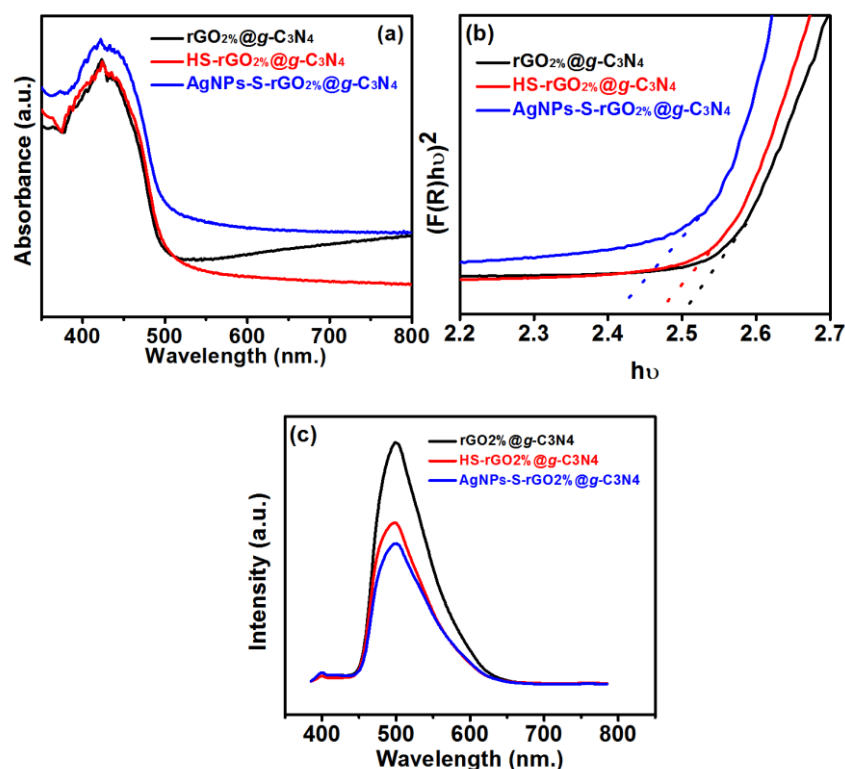


Figure 3. (a) UV-Visible absorption spectra (b) bandgap analysis and (c) PL spectra for $\text{rGO}_{2\%}@g\text{-C}_3\text{N}_4$, $\text{HS-rGO}_{2\%}@g\text{-C}_3\text{N}_4$, and $\text{AgNPs-S-rGO}_{2\%}@g\text{-C}_3\text{N}_4$.

3.3. Surface Chemical State Investigation

The C1s spectrum of $\text{rGO}_{2\%}@g\text{-C}_3\text{N}_4$ (Figure 4a) revealed three peaks at around 284.9, 285.8, and 288.6 eV accredited to the C=C, C=N, and C=O moieties, respectively [43,44], with contributions of 75.28%, 14.55%, and 10.17%. However, in thiolated $\text{HS-rGO}_{2\%}@g\text{-C}_3\text{N}_4$ and AgNPs coated composites ($\text{AgNPs-S-rGO}_{2\%}@g\text{-C}_3\text{N}_4$) (Figure 4b,c), the bonding

of detected elements was changed as reflected by changes in their spectra. The percentage contributions of C=C, C=N, and C=O changed to 70.38%, 18.69%, and 10.93%, respectively, in HS-rGO_{2%}@g-C₃N₄, while for AgNPs-S-rGO_{2%}@g-C₃N₄, they were 58.77%, 29.80% and 11.43%, respectively. The increase in C=O suggests that more anchoring sites are available to enhance catalytic activity [45]. Therefore, AgNPs-S-rGO_{2%}@g-C₃N₄ also has a high photocatalytic H₂ production rate in comparison to rGO_{2%}@g-C₃N₄ and HS-rGO_{2%}@g-C₃N₄ (Section 3.5). Further, Figure 4d shows the changes in C=C, C=N, and C=O of rGO_{2%}@g-C₃N₄, HS-rGO_{2%}@g-C₃N₄, and AgNPs-S-rGO_{2%}@g-C₃N₄.

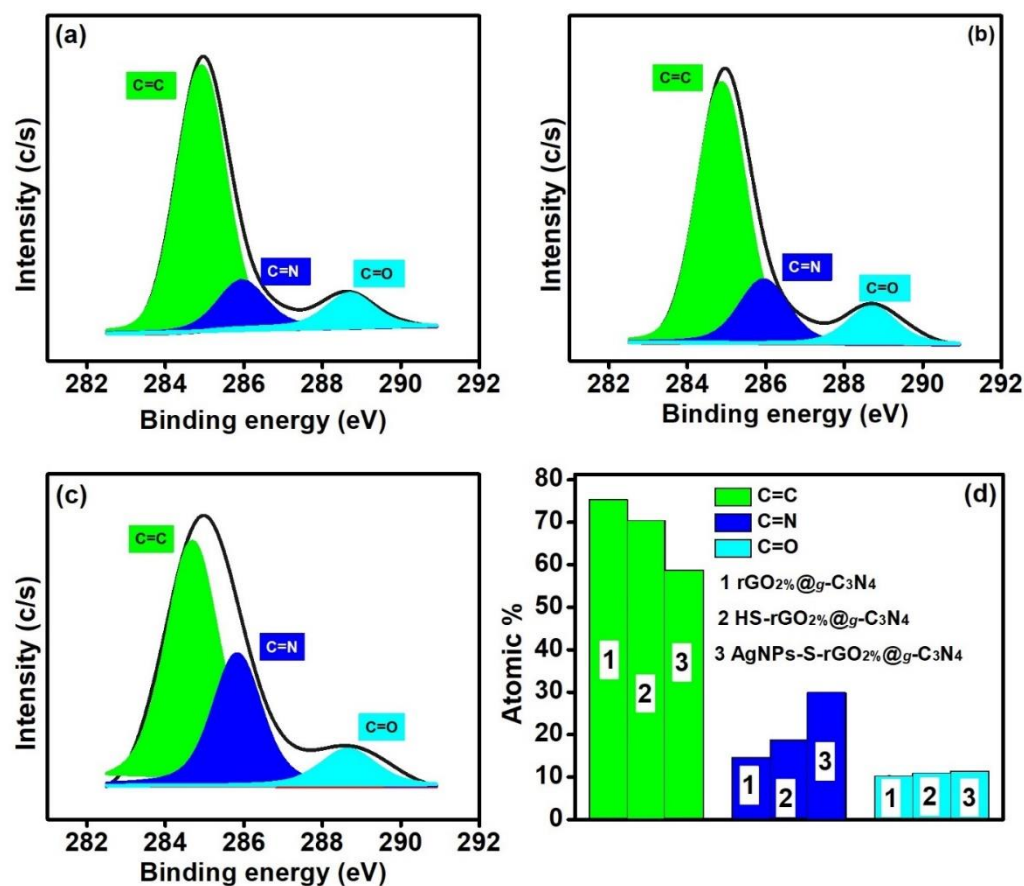


Figure 4. Chemical state analysis of C1s (a) rGO_{2%}@g-C₃N₄, (b) HS-rGO_{2%}@g-C₃N₄, (c) AgNPs-S-rGO_{2%}@g-C₃N₄ and (d) apparent change in functional groups for rGO_{2%}@g-C₃N₄, HS-rGO_{2%}@g-C₃N₄, and AgNPs-S-rGO_{2%}@g-C₃N₄.

The O1s spectra of the prepared materials provided evidence of oxygen intercalations. The peaks that appeared at around 529.2, 531.0 and 532.3 eV are attributed to lattice oxygen (O_i), carbon to oxygen bonding (C=O), and hydroxyl functional groups (OH), respectively [46,47]. The rGO_{2%}@g-C₃N₄ spectra showed the contribution of O_i to be around 38.82%, whereas the HS-rGO_{2%}@g-C₃N₄ and AgNPs-S-rGO_{2%}@g-C₃N₄ spectra contributed 19.49% and 36.78%, respectively (Figure 5a–c). The contribution of C=O was found to be maximised for AgNPs-S-rGO_{2%}@g-C₃N₄ and was 54.11%, which is according to the spectrum of C1s (Figure 5d). The percentage of OH was around 22.55%, 35.34% and 9.12% for rGO_{2%}@g-C₃N₄, HS-rGO_{2%}@g-C₃N₄ and AgNPs-S-rGO_{2%}@g-C₃N₄, respectively.

The S2p spectrum analysis of HS-rGO_{2%}@g-C₃N₄ (Figure 6a) shows two peaks at around 164.17 and 165.33 eV, attributed to the 2p_{3/2} and 2p_{1/2}, respectively, with a separation of 1.18 eV. However, after depositing the AgNPs on HS-rGO_{2%}@g-C₃N₄, the 2p_{3/2} and 2p_{1/2} peaks were shifted to 163.98 and 165.19, increasing the separation of 1.21 eV (Figure 6b). This change in the binding position of the 2p_{3/2} and 2p_{1/2} peaks revealed the interaction of the AgNPs with the sulphur group of HS-rGO_{2%}@g-C₃N₄.

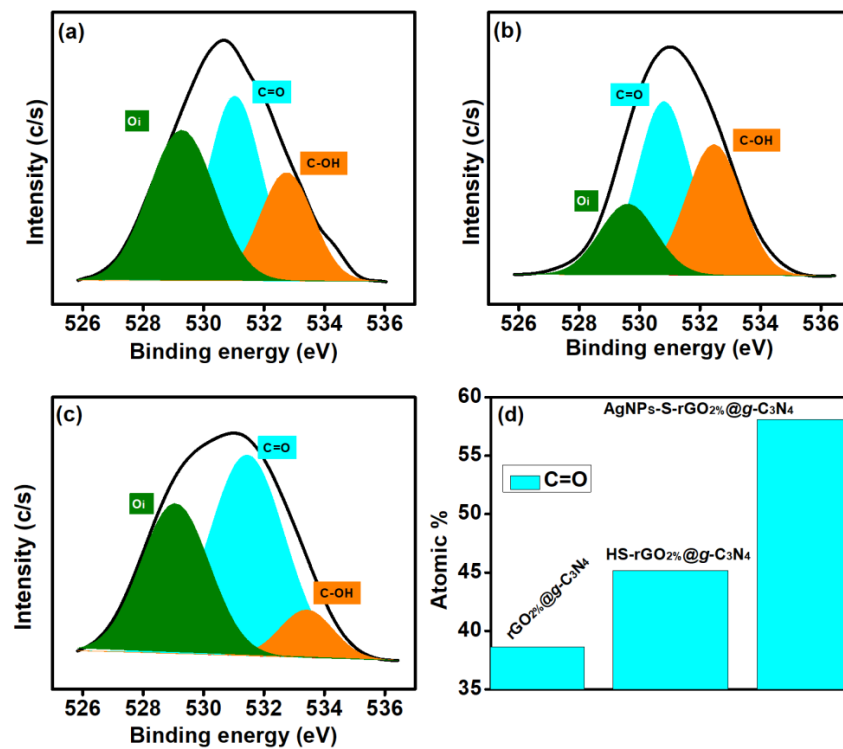


Figure 5. O1s-attached functional groups (a) $rGO_{2\%}@g-C_3N_4$, (b) $HS-rGO_{2\%}@g-C_3N_4$ (c) $AgNPs-S-rGO_{2\%}@g-C_3N_4$ and (d) increment in C=O bonding of $rGO_{2\%}@g-C_3N_4$, $HS-rGO_{2\%}@g-C_3N_4$, and $AgNPs-S-rGO_{2\%}@g-C_3N_4$.

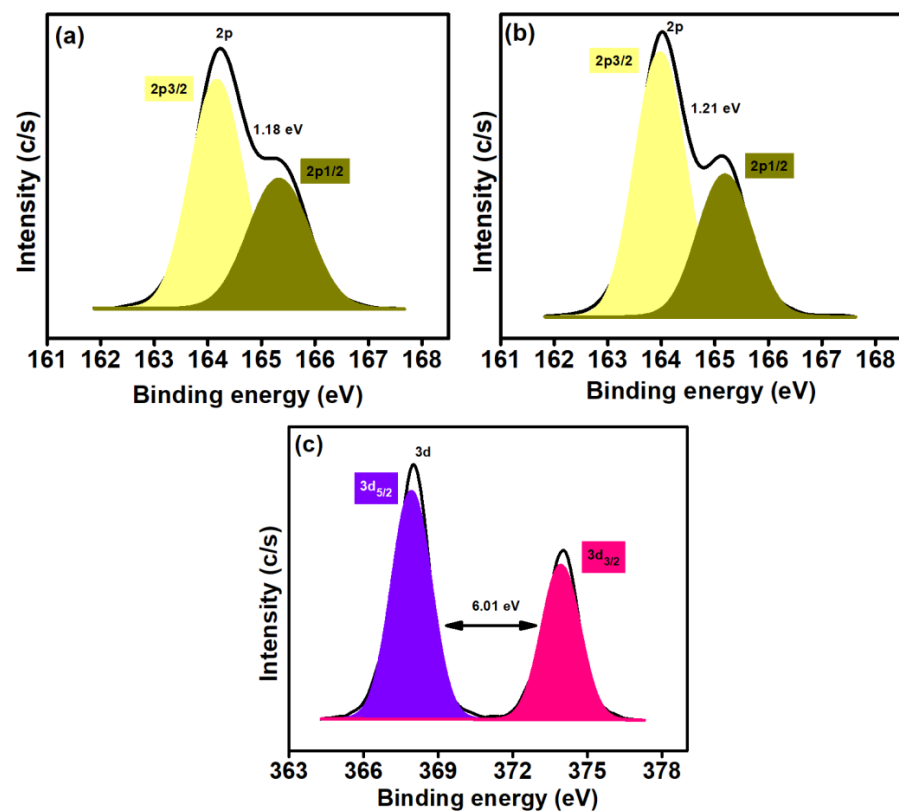


Figure 6. (a,b) S2p chemical state analysis of $HS-rGO_{2\%}@g-C_3N_4$ and $AgNPs-S-rGO_{2\%}@g-C_3N_4$ (c) Ag3d analysis for $AgNPs-S-rGO_{2\%}@g-C_3N_4$.

Furthermore, the Ag3d spectrum of AgNPs-S-rGO_{2%}@g-C₃N₄ (Figure 6c) was measured to explore the chemical nature of AgNPs. The peaks, which appeared at 367.93 and 373.93 eV, are attributed to Ag3d_{5/2} and Ag3d_{3/2}, respectively, which confirms the existence of zerovalent silver [48]. Moreover, zerovalent silver in AgNPs is highly desirable as it enhances the rate of photocatalytic reactions. In the present work, this property of silver is also responsible for accelerating hydrogen production [49].

3.4. Surface Morphology

The well-dispersed aqueous droplets of rGO_{2%}@g-C₃N₄, HS-rGO_{2%}@g-C₃N₄, and AgNPs-S-rGO_{2%}@g-C₃N₄ were drop-casted onto copper stubs and air-dried before scanning electron microscope (SEM) analysis was conducted. Likewise, for transmission electron microscope (TEM) analysis, the sample of AgNPs-S-rGO_{2%}@g-C₃N₄ was prepared by drop-casting it onto a copper-grid followed by air-drying. The morphology appearing in the SEM images of rGO_{2%}@g-C₃N₄, HS-rGO_{2%}@g-C₃N₄, and AgNPs-S-rGO_{2%}@g-C₃N₄ revealed that there is no interlayer stacking between g-C₃N₄ and rGO layers in their thiol-enriched (HS-rGO_{2%}@g-C₃N₄) and AgNP-decorated (AgNPs-S-rGO_{2%}@g-C₃N₄) composites compared to the non-functionalised (rGO_{2%}@g-C₃N₄) composite (Figure 7a–c).

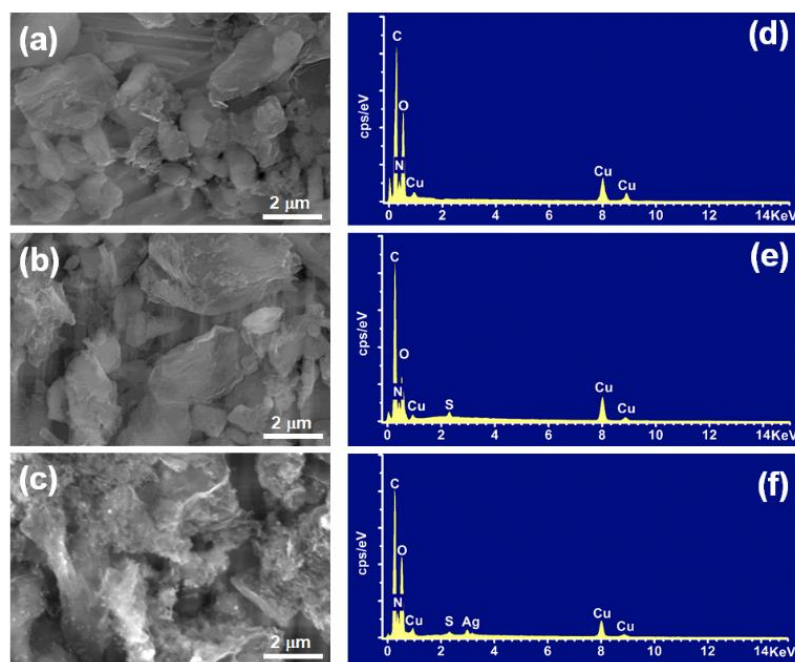


Figure 7. (a–c) SEM analysis and (d–f) EDS analysis of rGO_{2%}@g-C₃N₄, HS-rGO_{2%}@g-C₃N₄, and AgNPs-S-rGO_{2%}@g-C₃N₄.

In parallel (Figure 7d–f), the thiol peaks indicated in the EDX spectrum have also confirmed the thiol enrichment in HS-rGO_{2%}@g-C₃N₄. According to XPS studies, the engagement of these thiol groups with NaBH₄ reduced the silver ions under these experimental conditions, especially continuous sonication. It ensured the formation of AgNPs in the resulting AgNPs-S-rGO_{2%}@g-C₃N₄ composite. Briefly, small-sized AgNPs (less than 10 nm) were formed between the interlayer stacking of g-C₃N₄ and rGO in AgNPs-S-rGO_{2%}@g-C₃N₄, as seen in the TEM analysis shown in Figure 8.

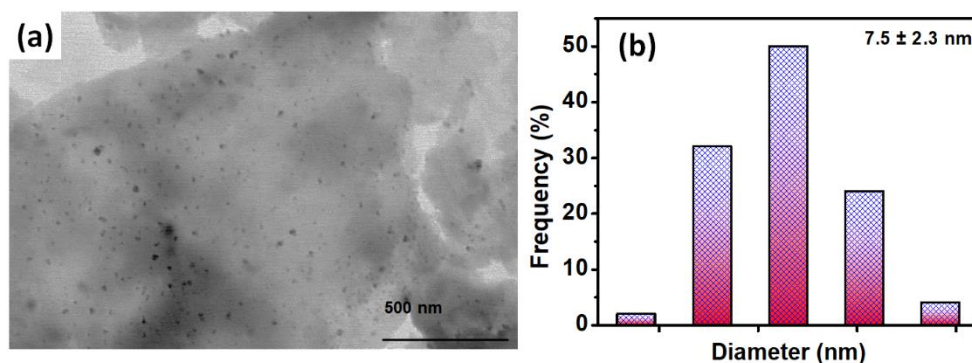


Figure 8. (a) Surface morphology of AgNPs-S-rGO_{2%}@g-C₃N₄ via TEM and (b) the estimated size of the AgNPs was 7.5 ± 2.3 measured using imageJ software.

3.5. Hydrogen Production and Proposed Mechanism for AgNPs-S-rGO_{2%}@g-C₃N₄

The photocatalytic H₂ production by g-C₃N₄ (Figure 9a) had a production rate of $555\text{-}\mu\text{mol g}^{-1}\text{ h}^{-1}$, and this low rate was accredited to the fast recombinations of charge carriers (electron-hole pair). This H₂ production rate of g-C₃N₄ was further improved with the addition of rGO. In rGO_{1%}@g-C₃N₄, the reaction rate increased to $886.66\text{ }\mu\text{mol g}^{-1}\text{ h}^{-1}$, which is 1.59 fold of g-C₃N₄. This increment in rate exhibited the contribution of rGO to accelerating the charge transfer efficiencies by tumbling the speedy recombinations of charge carriers. The role of rGO in increasing the H₂ production rate is consistent with the previous literature [50]. However, in these measurements, the H₂ production rate was reached $1369.86\text{ }\mu\text{mol g}^{-1}\text{ h}^{-1}$ with an increased weight percentage of rGO from 1% to 2% (rGO_{2%}@g-C₃N₄), which is 2.4-fold higher than the rate of g-C₃N₄. This was the maximum H₂ production rate achieved compared to 1, 3 and 4 wt.% loading of rGO and confirms the positive role of rGO as a co-catalyst in nanocomposites in enhancing catalytic performance. Thus, it is imperative to adjust the weight percentage of rGO in the subjected nanocomposites as its higher ratio can produce shielding effects, which ultimately reduces catalytic performance [51].

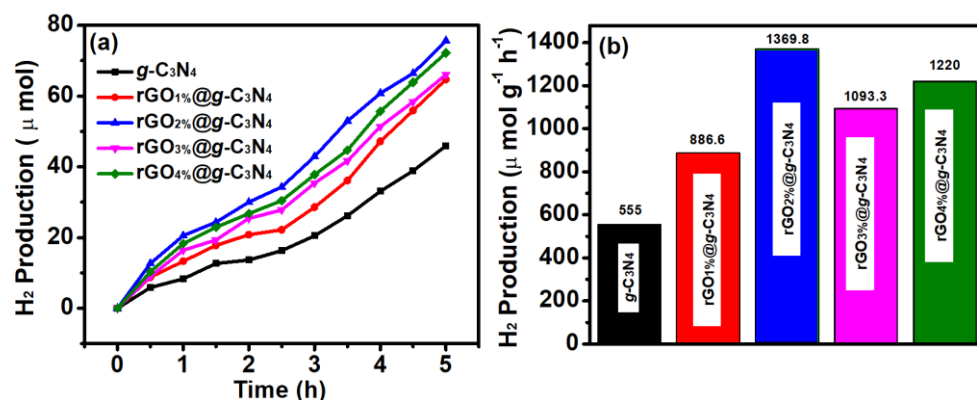


Figure 9. (a) H₂ production and (b) H₂ production rate per hour under the same experimental conditions for g-C₃N₄ and its composites with rGO at a concentration of 1 to 4 wt.%.

Therefore, the catalytic performance was reduced by further increasing the weight percentage of rGO to 3% and 4%. The rGO_{3%}@g-C₃N₄ showed H₂ production rate of $1220\text{ }\mu\text{mol g}^{-1}\text{ h}^{-1}$, whilst rGO_{4%}@g-C₃N₄ had a rate of $1093.33\text{ }\mu\text{mol g}^{-1}\text{ h}^{-1}$. This reduced hydrogen production above a specific weight percentage of added rGO is attributed to the light-shielding effect. This kind of result for a particular weight percentage of rGO has also been reported earlier [52]. Therefore, rGO_{2%}@g-C₃N₄ was selected as the most optimised sample for maximum hydrogen production under set experimental conditions. Figure 9b shows the change in the H₂ production rate with rGO to g-C₃N₄ at various concentrations

of rGO. The introduction of thiol groups (HS) could further increase the H₂ production rate of rGO_{2%}@g-C₃N₄. In addition, the groups can act as hole quenchers which also reduce the charge recombination ratio [53]. Therefore, HS-rGO_{2%}@g-C₃N₄ (after the thiolation of rGO_{2%}@g-C₃N₄), Figure 10a shows the H₂ production rate of 1745.23 μmol g⁻¹h⁻¹, which was 1.27 times higher than the rate of rGO_{2%}@g-C₃N₄. The HS groups have a strong affinity for noble transition metals; therefore, AgNPs were grown, using a chemical reduction method, over the surface of thiolated sheets of rGO_{2%}@g-C₃N₄, resulting in AgNPs-S-rGO_{2%}@g-C₃N₄. This AgNPs-S-rGO_{2%}@g-C₃N₄ (Figure 10a) was found to generate hydrogen at a rate of 3772.5 μmol g⁻¹h⁻¹, which is 2.16- and 2.76-fold higher than HS-rGO_{2%}@g-C₃N₄ and rGO_{2%}@g-C₃N₄, respectively. Moreover, Table 1 shows the ternary composites is better than binary composites for photocatalytic hydrogen production. These results also revealed the potential use of thiolated reduced graphene-oxide and graphitic carbon nitride with silver nanoparticles for enhanced photocatalytic hydrogen production from water.

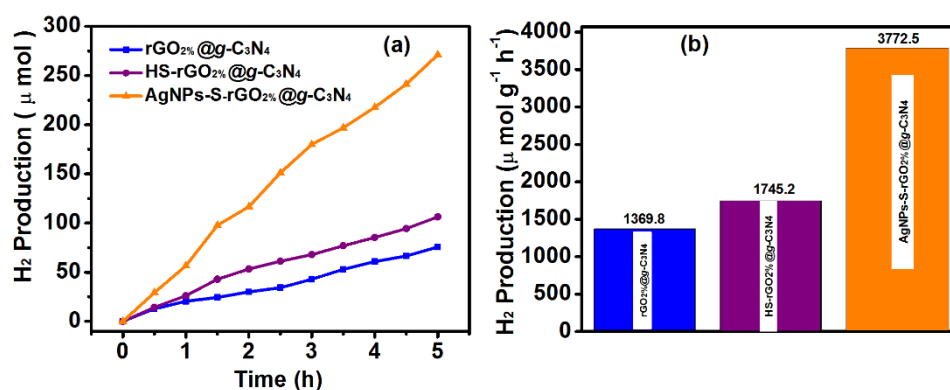


Figure 10. (a) Hydrogen production and (b) rate of hydrogen production per hour under the same set experimental conditions for rGO_{2%}@g-C₃N₄, HS-rGO_{2%}@g-C₃N₄ and AgNPs-S-rGO_{2%}@g-C₃N₄.

Table 1. Ternary composites of g-C₃N₄/rGO is better than binary composites for photocatalytic hydrogen production.

Binary Photocatalysts	Additive Co-Catalyst	Condition of Sacrificial Agent	Radiation Source	Maximum Hydrogen Yield (μmol h ⁻¹ g ⁻¹)	Reference with Year
Thiolated g-C ₃ N ₄ /rGO	Ag	Triethanolamine 15%	300 W Xenon lamp	3772.5	This work
g-C ₃ N ₄ /rGO	MoS ₂	Triethanolamine 0.1%	300 W Xenon lamp	317	[50] 2018
g-C ₃ N ₄ /rGO	MoS ₂	Sodium sulfite 0.25 Molar	450 Xenon lamp	1650	[54] 2017
g-C ₃ N ₄ /rGO	NiS ₂	Triethanolamine 1%	300 W Xenon lamp	1555.34	[25] 2019
g-C ₃ N ₄ /rGO	CoMoS ₂	Triethanolamine 1%	300 W Xenon lamp	684	[55] 2018
g-C ₃ N ₄ /rGO	CdS	Lactic acid 10%	350 W Xenon lamp	1000.5	[56] 2017

The stability of AgNPs-S-rGO_{2%}@g-C₃N₄ was also investigated by repeating the experiment under the same conditions for four cycles (Figure 11a). The AgNPs-S-rGO_{2%}@g-C₃N₄ was washed multiple times with ethanol and deionised water before starting each cycle. The efficiency of the AgNPs-S-rGO_{2%}@g-C₃N₄ (Figure 11b) remained at 96% even after four cycles, supporting the reusability of the synthesised AgNPs-S-rGO_{2%}@g-C₃N₄ catalyst.

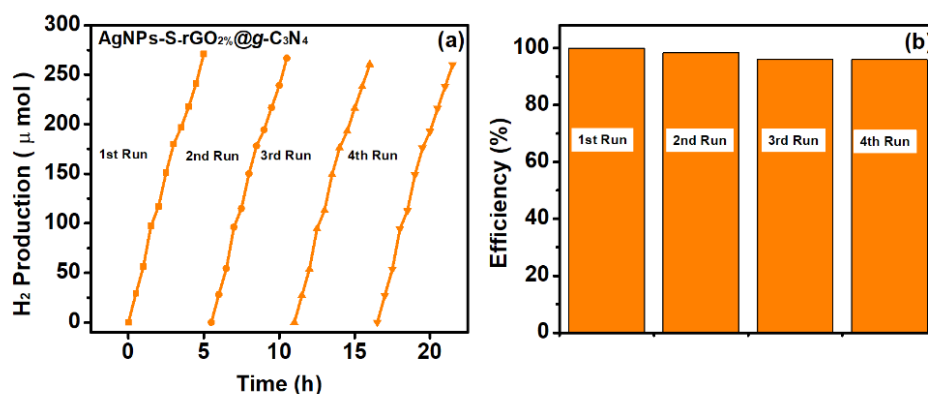


Figure 11. (a,b) Reusability and stability of AgNPs-S-rGO_{2%}@g-C₃N₄ for four consecutive cycles.

The photocatalytic production of H₂, illustrated in Figure 12, elaborates that, in AgNPs-S-rGO_{2%}@g-C₃N₄, the electrons (e⁻) in the VB of g-C₃N₄ were excited by visible light to the CB, leaving behind holes (h⁺) in the VB. The incorporation of AgNPs in this composite also helped absorb light due to their characteristic SPR and improved the catalytic activity by reducing the recombination of photogenerated electrons and holes. The photoexcited e⁻ in CB of g-C₃N₄ reacted with water molecules adhered to its surface and generated hydrogen gas. Meanwhile, some of the e⁻ in the CB of the g-C₃N₄ were transferred to the CB of rGO. Similar to g-C₃N₄, these electrons (e⁻) in the CB of the rGO also reduced water to H₂. At the same time, the h⁺ generated in the g-C₃N₄ oxidised the existing species of hydroxides to water and oxygen molecules.

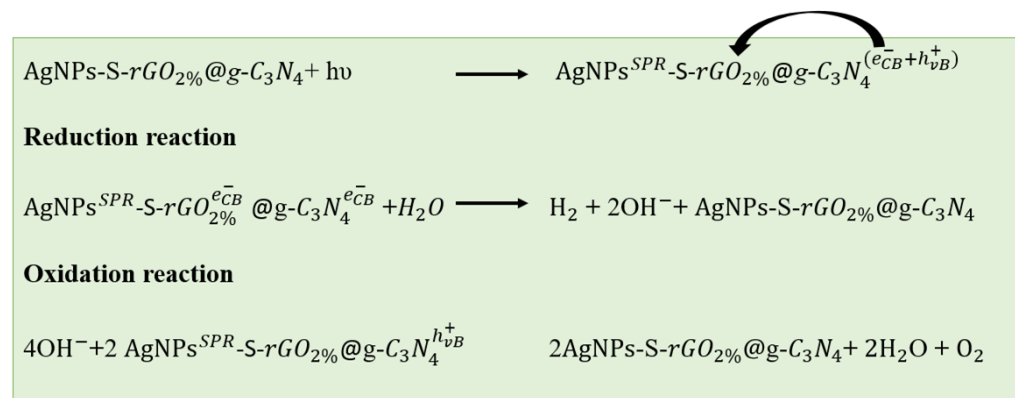


Figure 12. Proposed enhanced hydrogen production mechanism of AgNPs-S-rGO_{2%}@g-C₃N₄.

3.6. Photocatalytic CIP Degradation

The UV-absorption spectra (Figure 13a) of CIP antibiotics (25 mg/L and pH 7) showed the appearance of the maximum absorption at 274 nm, which is the characterises peak of CIP [57]. This absorption continued down with the increase in the irradiation time. The % removal of CIP with and without a catalyst is shown in Figure 13b. The results revealed 2% removal of CIP in the absence of rGO_{2%}@g-C₃N₄ (photolysis) which also indicated the stability of CIP [58]. However, after adding rGO_{2%}@g-C₃N₄, its degradation was started and reached 83.29% within 70 min by irradiating under visible light (400 nm, 150 watts). These results well exposed the potential benefit of rGO_{2%}@g-C₃N₄ photocatalyst for the removal of CIP from contaminated water. The CIP degradation was further enhanced to 90.29% and 95.90% with HS-rGO_{2%}@g-C₃N₄ and AgNPs-S-rGO_{2%}@g-C₃N₄, respectively. The reaction rate was 0.02555, 0.03331 and 0.04564, respectively, for rGO_{2%}@g-C₃N₄, HS-rGO_{2%}@g-C₃N₄ and AgNPs-S-rGO_{2%}@g-C₃N₄. It is inferred that the reaction rate has reached a maximum value for AgNPs-S-rGO_{2%}@g-C₃N₄ (Figure 13c,d). Generally, the degradation ability by catalytic systems depends on various factors such as its band gap, charge carries recombination ratio etc.

The bandgap of AgNPs-S-rGO_{2%}@g-C₃N₄ was (2.42 eV) which is less in comparison to HS-rGO_{2%}@g-C₃N₄ (2.46 eV) and rGO_{2%}@g-C₃N₄ (2.50 eV). This indicates that the conduction of charge carrier is high for AgNPs-S-rGO_{2%}@g-C₃N₄ in comparison to HS-rGO_{2%}@g-C₃N₄ and rGO_{2%}@g-C₃N₄. Moreover, PL analysis (Figure 3C) also indicated the separation of charge-recombination ratios for AgNPs-S-rGO_{2%}@g-C₃N₄ while moving towards the conduction band. This supports accelerating the conduction of charge carriers, ultimately producing the hydroxyl, reactive oxygen species and super radical oxides supporting CIP's enhanced degradation [59].

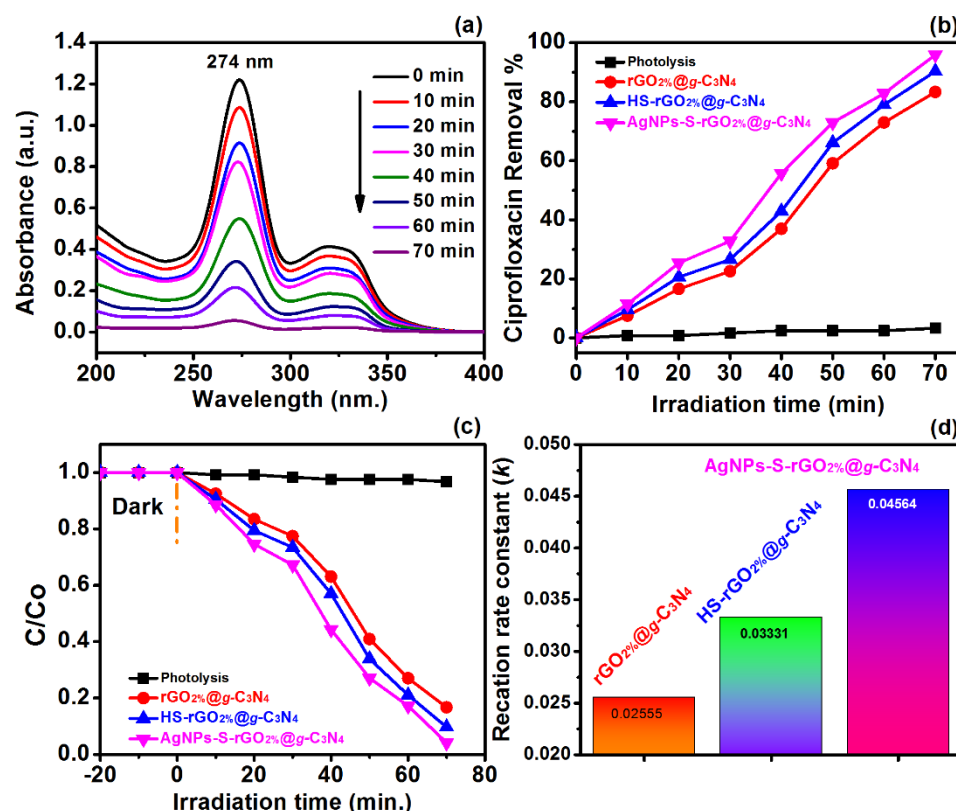


Figure 13. (a) UV-Absorption spectra of CIP (b) percentage removal of CIP with and without a catalyst (c,d) reaction rate constant for CIP degradation.

Effect of AgNPs-S-rGO_{2%}@g-C₃N₄ Dosage over CIP Degradation

The effect of heterogeneous catalyst dosage may change the reaction rate and efficiency of the photocatalytic process. Therefore, further investigation was carried out at different catalyst dosages of AgNPs-S-rGO_{2%}@g-C₃N₄ while keeping the other reaction parameters such as irradiation time, pH and dye concentrations constant. In this regard, 15 mg/L, 25, 35 and 45 mg/L of AgNPs-S-rGO_{2%}@g-C₃N₄ was selected while keeping the CIP concentration fixed, i.e., 25 mg/L and pH was kept constant at 6. The results indicated (Figure 14) the enhanced photocatalytic degradation of CIP, when the dosage of AgNPs-S-rGO_{2%}@g-C₃N₄ increased from 15 mg/L to 25 mg/L. However, after increasing the dosage of AgNPs-S-rGO_{2%}@g-C₃N₄ from 25 mg/L, 35, and 45 mg/L, a decline in CIP degradation was noticed. Therefore, maximum CIP degradation was found 84.87%, 95.90%, 88.22% and 87.27%, respectively, for 15 mg/L, 25, 35, and 45 mg/L. These results indicated that the optimal value of AgNPs-S-rGO_{2%}@g-C₃N₄ was 25 mg/L necessary to obtain the maximum degradation of CIP at pH 6. With an increase in the photocatalyst dosage, an obvious increase in the reactive/reaction sites occurred, leading to a high CIP's photocatalytic degradation rate. This enhanced degradation was attributed to the increase in hydroxyl radical while irradiation. However, a high catalyst dosage of AgNPs-S-rGO_{2%}@g-C₃N₄ beyond its optimal value might lead to suspension opacity, which possibly increased the light scattering inside

the reactor and low infiltration of phonons. These factors will eventually decrease the catalytic rate due to the less active catalyst present in the reactor. It can be stated that when present in high concentrations, the catalyst nanoparticles become agglomerated, leading to a decrease in the available reactive active sites. Further deactivation of active catalyst might occur due to the bombardment of activating molecules with molecules at the ground state, which resulted in the decrease of photocatalytic efficiency [60].

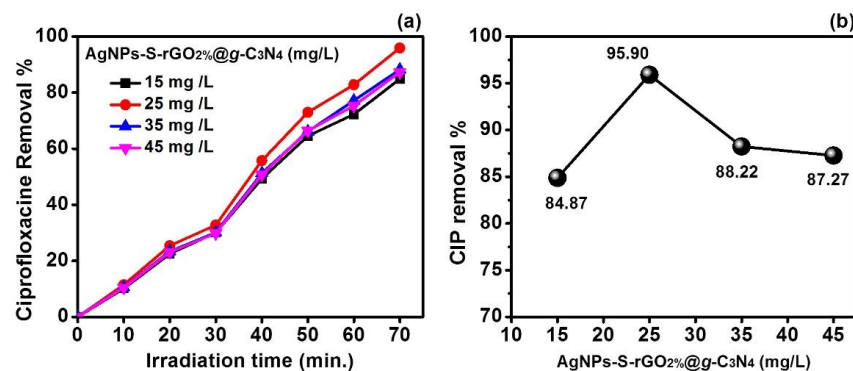


Figure 14. (a,b) Effect of AgNPs-S-rGO_{2%}@g-C₃N₄ dosage over CIP degradation at constant CIP concentration (25 mg/L) and constant pH-6.

4. Conclusions

The ratio of rGO to g-C₃N₄ has a fundamental impact on the photocatalytic CIP degradation and H₂ production rate. The optimal concentration of rGO will curb the charge recombination ratio of the charged particles at the interface of their heterojunctions. Therefore, the optimum concentration of rGO, i.e., 2 wt.%, in the composite rGO_{2%}@g-C₃N₄, exhibited the maximum H₂ production rate. Furthermore, the thiolation of rGO and g-C₃N₄ in HS-rGO_{2%}@g-C₃N₄ also overcame the negative shielding effect of rGO. It decreased the bandgap, building the capability to absorb more photons, which is favourable for enhanced catalytic activity. Moreover, shifting the diffraction peaks for planes of thiolated rGO and g-C₃N₄ indicated a successful interaction between thiolated functional groups and AgNPs, as confirmed by XPS studies. This interaction also formed smaller AgNPs, keeping the layered assemblies of AgNPs-S-rGO_{2%}@g-C₃N₄ intact, stable and exfoliated. Moreover, C1s and O1s spectra revealed the fundamental role of C=O in the enhanced CIP and hydrogen production activity of AgNPs-S-rGO_{2%}@g-C₃N₄ compared to HS-rGO_{2%}@g-C₃N₄ and rGO_{2%}@g-C₃N₄, which were 3772.5, 1745.2, and 1369.8 μmol g⁻¹h⁻¹, respectively, under the experimental conditions.

Supplementary Materials: The following supporting information can be downloaded at <https://www.mdpi.com/article/10.3390/polym14071290/s1>, Figure S1: Comparison of PL spectra for pure g-C₃N₄, its composites with rGO at various concentrations of rGO, further its thiolated composites (HS-rGO_{2%}@g-C₃N₄) and AgNPs decorated thiolated composites (AgNPs-S-rGO_{2%}@g-C₃N₄), Figure S2: XPS survey spectra for rGO_{2%}@g-C₃N₄, HS-rGO_{2%}@g-C₃N₄, and AgNPs-S-rGO_{2%}@g-C₃N₄, Table S1: XPS Elemental composition of AgNPs-S-rGO_{2%}@g-C₃N₄ Survey Spectra.

Author Contributions: Conceptualization A.J. and S.Z.H.; Methodology A.J., S.Z.H., A.A.M. and N.H.A.-H.; Formal analysis A.J. and S.Z.H.; Writing—original draft A.J. and S.Z.H.; Funding acquisition N.H.A.-H.; Writing—review editing A.J. and A.A.M. All authors have read and agreed to the published version of the manuscript.

Funding: The authors extend their appreciation to the Deputyship for Research and Innovation, Ministry of Education in Saudi Arabia for funding this research work through the project number IFPHI-169-135-2020 and King Abdulaziz University, DSR, Jeddah, Saudi Arabia.

Institutional Review Board Statement: Not applicable.

Informed Consent Statement: Not applicable.

Data Availability Statement: The data presented in this study are available on request from the corresponding author.

Acknowledgments: The authors extend their appreciation to the Deputyship for Research and Innovation, Ministry of Education in Saudi Arabia for funding this research work through the project number IFPHI-169-135-2020" and King Abdulaziz University, DSR, Jeddah, Saudi Arabia.

Conflicts of Interest: There is no conflict of interest to declare for this research.

References

1. Zhu, J.; Zäch, M. Nanostructured materials for photocatalytic hydrogen production. *Curr. Opin. Colloid Interface Sci.* **2009**, *14*, 260–269. [[CrossRef](#)]
2. Han, H.S.; Park, W.; Sivanantham, A.; Hwang, S.W.; Surendran, S.; Sim, U.; Cho, I.S. Facile fabrication of nanotubular heterostructure for enhanced photoelectrochemical performance. *Ceram. Int.* **2021**, *47*, 3972–3977. [[CrossRef](#)]
3. Saraswat, S.K.; Rodene, D.D.; Gupta, R.B. Recent advancements in semiconductor materials for photoelectrochemical water splitting for hydrogen production using visible light. *Renew. Sustain. Energy Rev.* **2018**, *89*, 228–248. [[CrossRef](#)]
4. Chen, Y.-C.; Huang, Y.-S.; Huang, H.; Su, P.-J.; Perng, T.-P.; Chen, L.-J. Photocatalytic enhancement of hydrogen production in water splitting under simulated solar light by band gap engineering and localized surface plasmon resonance of ZnxCd1-xS nanowires decorated by Au nanoparticles. *Nano Energy* **2020**, *67*, 104225. [[CrossRef](#)]
5. Han, H.S.; Park, W.; Hwang, S.W.; Kim, H.; Sim, Y.; Surendran, S.; Sim, U.; Cho, I.S. (020)-Textured tungsten trioxide nanostructure with enhanced photoelectrochemical activity. *J. Catal.* **2020**, *389*, 328–336. [[CrossRef](#)]
6. Amirav, L.; Alivisatos, A.P. Photocatalytic Hydrogen Production with Tunable Nanorod Heterostructures. *J. Phys. Chem. Lett.* **2010**, *1*, 1051–1054. [[CrossRef](#)]
7. Muthurasu, A.; Ojha, G.P.; Lee, M.; Kim, H.Y. Integration of Cobalt Metal-Organic Frameworks into an Interpenetrated Prussian Blue Analogue to Derive Dual Metal-Organic Framework-Assisted Cobalt Iron Derivatives for Enhancing Electrochemical Total Water Splitting. *J. Phys. Chem. C* **2020**, *124*, 14465–14476. [[CrossRef](#)]
8. Singla, S.; Sharma, S.; Basu, S.; Shetti, N.P.; Reddy, K.R. Graphene/graphitic carbon nitride-based ternary nanohybrids: Synthesis methods, properties, and applications for photocatalytic hydrogen production. *FlatChem* **2020**, *24*, 100200. [[CrossRef](#)]
9. Bouyarmane, H.; El Bekkali, C.; Labrag, J.; Es-saidi, I.; Bouhnik, O.; Abdelmoumen, H.; Laghizil, A.; Nunzi, J.M.; Robert, D. Photocatalytic degradation of emerging antibiotic pollutants in waters by TiO₂/Hydroxyapatite nanocomposite materials. *Surf. Interfaces* **2021**, *24*, 101155. [[CrossRef](#)]
10. Ding, Q.; Lam, F.L.Y.; Hu, X. Complete degradation of ciprofloxacin over g-C₃N₄-iron oxide composite via heterogeneous dark Fenton reaction. *J. Environ. Manag.* **2019**, *244*, 23–32. [[CrossRef](#)]
11. Das, K.K.; Patnaik, S.; Mansingh, S.; Behera, A.; Mohanty, A.; Acharya, C.; Parida, K.M. Enhanced photocatalytic activities of polypyrrole sensitized zinc ferrite/graphitic carbon nitride n-n heterojunction towards ciprofloxacin degradation, hydrogen evolution and antibacterial studies. *J. Colloid Interface Sci.* **2020**, *561*, 551–567. [[CrossRef](#)] [[PubMed](#)]
12. Wang, J.; Sun, Y.; Fu, L.; Sun, Z.; Ou, M.; Zhao, S.; Chen, Y.; Yu, F.; Wu, Y. A defective g-C₃N₄/RGO/TiO₂ composite from hydrogen treatment for enhanced visible-light photocatalytic H₂ production. *Nanoscale* **2020**, *12*, 22030–22035. [[CrossRef](#)] [[PubMed](#)]
13. Cao, S.; Fan, B.; Feng, Y.; Chen, H.; Jiang, F.; Wang, X. Sulfur-doped g-C₃N₄ nanosheets with carbon vacancies: General synthesis and improved activity for simulated solar-light photocatalytic nitrogen fixation. *Chem. Eng. J.* **2018**, *353*, 147–156. [[CrossRef](#)]
14. Sun, J.; Yang, S.; Liang, Z.; Liu, X.; Qiu, P.; Cui, H.; Tian, J. Two-dimensional/one-dimensional molybdenum sulfide (MoS₂) nanoflake/graphitic carbon nitride (g-C₃N₄) hollow nanotube photocatalyst for enhanced photocatalytic hydrogen production activity. *J. Colloid Interface Sci.* **2020**, *567*, 300–307. [[CrossRef](#)]
15. Lim, Y.; Lee, D.-K.; Kim, S.M.; Park, W.; Cho, S.Y.; Sim, U. Low Dimensional Carbon-Based Catalysts for Efficient Photocatalytic and Photo/Electrochemical Water Splitting Reactions. *Materials* **2019**, *13*, 114. [[CrossRef](#)]
16. Xu, L.; Huang, W.-Q.; Wang, L.-L.; Tian, Z.-A.; Hu, W.; Ma, Y.; Wang, X.; Pan, A.; Huang, G.-F. Insights into Enhanced Visible-Light Photocatalytic Hydrogen Evolution of g-C₃N₄ and Highly Reduced Graphene Oxide Composite: The Role of Oxygen. *Chem. Mater.* **2015**, *27*, 1612–1621. [[CrossRef](#)]
17. Ojha, G.P.; Pant, B.; Park, S.-J.; Park, M.; Kim, H.-Y. Synthesis and characterization of reduced graphene oxide decorated with CeO₂-doped MnO₂ nanorods for supercapacitor applications. *J. Colloid Interface Sci.* **2017**, *494*, 338–344. [[CrossRef](#)]
18. Jilani, A.; Rehman, G.U.; Ansari, M.O.; Othman, M.H.D.; Hussain, S.Z.; Dustgeer, M.R.; Darwesh, R. Sulfonated polyaniline-encapsulated graphene@graphitic carbon nitride nanocomposites for significantly enhanced photocatalytic degradation of phenol: A mechanistic study. *New J. Chem.* **2020**, *44*, 19570–19580. [[CrossRef](#)]
19. Liu, G.; Niu, P.; Sun, C.; Smith, S.C.; Chen, Z.; Lu, G.Q.; Cheng, H.-M. Unique Electronic Structure Induced High Photoreactivity of Sulfur-Doped Graphitic C₃N₄. *J. Am. Chem. Soc.* **2010**, *132*, 11642–11648. [[CrossRef](#)]
20. Raheman Ar, S.; Wilson, H.M.; Momin, B.M.; Annapure, U.S.; Jha, N. CdSe quantum dots modified thiol functionalized g-C₃N₄: Intimate interfacial charge transfer between 0D/2D nanostructure for visible light H₂ evolution. *Renew. Energy* **2020**, *158*, 431–443. [[CrossRef](#)]

21. Jiao, J.; Wan, J.; Ma, Y.; Wang, Y. Facile formation of silver nanoparticles as plasmonic photocatalysts for hydrogen production. *RSC Adv.* **2016**, *6*, 106031–106034. [[CrossRef](#)]
22. Gao, M.; Sun, L.; Wang, Z.; Zhao, Y. Controlled synthesis of Ag nanoparticles with different morphologies and their antibacterial properties. *Mater. Sci. Eng. C* **2013**, *33*, 397–404. [[CrossRef](#)]
23. Jaiswal, A.; Pal, S.; Kumar, A.; Prakash, R. Metal free triad from red phosphorous, reduced graphene oxide and graphitic carbon nitride (red P-rGO-g-C₃N₄) as robust electro-catalysts for hydrogen evolution reaction. *Electrochim. Acta* **2020**, *338*, 135851. [[CrossRef](#)]
24. Ibrahim, Y.O.; Hezam, A.; Qahtan, T.F.; Al-Aswad, A.H.; Gondal, M.A.; Drmosh, Q.A. Laser-assisted synthesis of Z-scheme TiO₂/rGO/g-C₃N₄ nanocomposites for highly enhanced photocatalytic hydrogen evolution. *Appl. Surf. Sci.* **2020**, *534*, 147578. [[CrossRef](#)]
25. Pan, J.; Wang, B.; Dong, Z.; Zhao, C.; Jiang, Z.; Song, C.; Wang, J.; Zheng, Y.; Li, C. The 2D RGO-NiS₂ dual co-catalyst synergistic modified g-C₃N₄ aerogel towards enhanced photocatalytic hydrogen production. *Int. J. Hydrogen Energy* **2019**, *44*, 19942–19952. [[CrossRef](#)]
26. Jilani, A.; Othman, M.H.D.; Ansari, M.O.; Kumar, R.; Alshahrie, A.; Ismail, A.F.; Khan, I.U.; Sajith, V.K.; Barakat, M.A. Facile spectroscopic approach to obtain the optoelectronic properties of few-layered graphene oxide thin films and their role in photocatalysis. *New J. Chem.* **2017**, *41*, 14217–14227. [[CrossRef](#)]
27. Chua, C.K.; Pumera, M. Monothiolation and Reduction of Graphene Oxide via One-Pot Synthesis: Hybrid Catalyst for Oxygen Reduction. *ACS Nano* **2015**, *9*, 4193–4199. [[CrossRef](#)]
28. Zhang, Y.; Pan, Q.; Chai, G.; Liang, M.; Dong, G.; Zhang, Q.; Qiu, J. Synthesis and luminescence mechanism of multicolor-emitting g-C₃N₄ nanopowders by low temperature thermal condensation of melamine. *Sci. Rep.* **2013**, *3*, 1943. [[CrossRef](#)]
29. Jilani, A.; Ansari, M.O.; Rehman, G.u.; Shakoob, M.B.; Hussain, S.Z.; Othman, M.H.D.; Ahmad, S.R.; Dustgeer, M.R.; Alshahrie, A. Phenol removal and hydrogen production from water: Silver nanoparticles decorated on polyaniline wrapped zinc oxide nanorods. *J. Ind. Eng. Chem.* **2022**, in press. [[CrossRef](#)]
30. Mudassir, M.A.; Hussain, S.Z.; Jilani, A.; Zhang, H.; Ansari, T.M.; Hussain, I. Magnetic Hierarchically Macroporous Emulsion-Templated Poly(acrylic acid)–Iron Oxide Nanocomposite Beads for Water Remediation. *Langmuir* **2019**, *35*, 8996–9003. [[CrossRef](#)]
31. Dai, K.; Lu, L.; Liu, Q.; Zhu, G.; Wei, X.; Bai, J.; Xuan, L.; Wang, H. Sonication assisted preparation of graphene oxide/graphitic-C₃N₄ nanosheet hybrid with reinforced photocurrent for photocatalyst applications. *Dalton Trans.* **2014**, *43*, 6295–6299. [[CrossRef](#)] [[PubMed](#)]
32. Dong, F.; Wu, L.; Sun, Y.; Fu, M.; Wu, Z.; Lee, S.C. Efficient synthesis of polymeric g-C₃N₄ layered materials as novel efficient visible light driven photocatalysts. *J. Mater. Chem.* **2011**, *21*, 15171–15174. [[CrossRef](#)]
33. Liu, S.-H.; Tang, W.-T.; Chou, P.-H. Microwave-assisted synthesis of triple 2D g-C₃N₄/Bi₂WO₆/rGO composites for ibuprofen photodegradation: Kinetics, mechanism and toxicity evaluation of degradation products. *Chem. Eng. J.* **2020**, *387*, 124098. [[CrossRef](#)]
34. Yao, X.; Zhang, W.; Huang, J.; Du, Z.; Hong, X.; Chen, X.; Hu, X.; Wang, X. Enhanced photocatalytic nitrogen fixation of Ag/B-doped g-C₃N₄ nanosheets by one-step in-situ decomposition-thermal polymerization method. *Appl. Catal. A Gen.* **2020**, *601*, 117647. [[CrossRef](#)]
35. Amendola, V. Surface plasmon resonance of silver and gold nanoparticles in the proximity of graphene studied using the discrete dipole approximation method. *Phys. Chem. Chem. Phys.* **2016**, *18*, 2230–2241. [[CrossRef](#)]
36. Cai, W.; Zhang, Y.; Jia, J.; Zhang, L. Semiconducting optical properties of silver/silica mesoporous composite. *Appl. Phys. Lett.* **1998**, *73*, 2709–2711. [[CrossRef](#)]
37. Yuan, J.; Yi, X.; Tang, Y.; Liu, C.; Luo, S. Efficient Photocatalytic Hydrogen Evolution and CO₂ Reduction: Enhanced Light Absorption, Charge Separation, and Hydrophilicity by Tailoring Terminal and Linker Units in g-C₃N₄. *ACS Appl. Mater. Interfaces* **2020**, *12*, 19607–19615. [[CrossRef](#)]
38. Hu, K.; Yao, M.; Yang, Z.; Xiao, G.; Zhu, L.; Zhang, H.; Liu, R.; Zou, B.; Liu, B. Pressure tuned photoluminescence and band gap in two-dimensional layered g-C₃N₄: The effect of interlayer interactions. *Nanoscale* **2020**, *12*, 12300–12307. [[CrossRef](#)]
39. Li, Y.; Zhang, H.; Liu, P.; Wang, D.; Li, Y.; Zhao, H. Cross-Linked g-C₃N₄/rGO Nanocomposites with Tunable Band Structure and Enhanced Visible Light Photocatalytic Activity. *Small* **2013**, *9*, 3336–3344. [[CrossRef](#)]
40. Li, W.; Rodríguez-Castellón, E.; Bandoz, T.J. Photosensitivity of g-C₃N₄/S-doped carbon composites: Study of surface stability upon exposure to CO₂ and/or water in ambient light. *J. Mater. Chem. A* **2017**, *5*, 24880–24891. [[CrossRef](#)]
41. Jo, W.-K.; Kumar, S.; Eslava, S.; Tonda, S. Construction of Bi₂WO₆/RGO/g-C₃N₄ 2D/2D/2D hybrid Z-scheme heterojunctions with large interfacial contact area for efficient charge separation and high-performance photoreduction of CO₂ and H₂O into solar fuels. *Appl. Catal. B Environ.* **2018**, *239*, 586–598. [[CrossRef](#)]
42. Zhang, N.; Yang, M.-Q.; Tang, Z.-R.; Xu, Y.-J. Toward Improving the Graphene–Semiconductor Composite Photoactivity via the Addition of Metal Ions as Generic Interfacial Mediator. *ACS Nano* **2014**, *8*, 623–633. [[CrossRef](#)] [[PubMed](#)]
43. Yan, X.; Xu, T.; Chen, G.; Yang, S.; Liu, H.; Xue, Q. Preparation and characterization of electrochemically deposited carbon nitride films on silicon substrate. *J. Phys. D Appl. Phys.* **2004**, *37*, 907–913. [[CrossRef](#)]
44. Zheng, Y.; Yang, Y.; Zhang, Y.; Zou, W.; Luo, Y.; Dong, L.; Gao, B. Facile one-step synthesis of graphitic carbon nitride-modified biochar for the removal of reactive red 120 through adsorption and photocatalytic degradation. *Biochar* **2019**, *1*, 89–96. [[CrossRef](#)]

45. Cao, S.; Yu, J. Carbon-based H₂-production photocatalytic materials. *J. Photochem. Photobiol. C Photochem. Rev.* **2016**, *27*, 72–99. [[CrossRef](#)]
46. John, F.; William, F.; Peter, E.; Kenneth, D. *Handbook of X-ray Photoelectron Spectroscopy*; Physical Electronics Inc.: Chanhassen, MN, USA, 1995.
47. Das, S.K.; Dickinson, C.; Lafir, F.; Brougham, D.F.; Marsili, E. Synthesis, characterization and catalytic activity of gold nanoparticles biosynthesized with *Rhizopus oryzae* protein extract. *Green Chem.* **2012**, *14*, 1322–1334. [[CrossRef](#)]
48. Zhang, S.; Hu, L.; Wang, H.; Feng, D. The anti-seizure effect of Ag nanoparticles additive in multialkylated cyclopentanes oil under vacuum condition. *Tribol. Int.* **2012**, *55*, 1–6. [[CrossRef](#)]
49. Kumar, R.; Rashid, J.; Barakat, M.A. Zero valent Ag deposited TiO₂ for the efficient photocatalysis of methylene blue under UV-C light irradiation. *Colloids Interface Sci. Commun.* **2015**, *5*, 1–4. [[CrossRef](#)]
50. Yuan, Y.-J.; Yang, Y.; Li, Z.; Chen, D.; Wu, S.; Fang, G.; Bai, W.; Ding, M.; Yang, L.-X.; Cao, D.-P.; et al. Promoting Charge Separation in g-C₃N₄/Graphene/MoS₂ Photocatalysts by Two-Dimensional Nanojunction for Enhanced Photocatalytic H₂ Production. *ACS Appl. Energy Mater.* **2018**, *1*, 1400–1407. [[CrossRef](#)]
51. Ong, W.-J.; Tan, L.-L.; Chai, S.-P.; Yong, S.-T.; Mohamed, A.R. Surface charge modification via protonation of graphitic carbon nitride (g-C₃N₄) for electrostatic self-assembly construction of 2D/2D reduced graphene oxide (rGO)/g-C₃N₄ nanostructures toward enhanced photocatalytic reduction of carbon dioxide to methane. *Nano Energy* **2015**, *13*, 757–770. [[CrossRef](#)]
52. Lewandowska-Andralojc, A.; Malolepszy, A.; Stritt, A.; Grohmann, A. Modification of eosin Y and cobalt molecular catalyst system with reduced graphene oxide for enhanced photocatalytic hydrogen production. *Catal. Sci. Technol.* **2020**, *10*, 4693–4702. [[CrossRef](#)]
53. Das, S.; Dutta, A.; Bera, R.; Patra, A. Ultrafast carrier dynamics in 2D-2D hybrid structures of functionalized GO and CdSe nanoplatelets. *Phys. Chem. Chem. Phys.* **2019**, *21*, 15568–15575. [[CrossRef](#)] [[PubMed](#)]
54. Wang, M.; Ju, P.; Li, J.; Zhao, Y.; Han, X.; Hao, Z. Facile Synthesis of MoS₂/g-C₃N₄/GO Ternary Heterojunction with Enhanced Photocatalytic Activity for Water Splitting. *ACS Sustain. Chem. Eng.* **2017**, *5*, 7878–7886. [[CrossRef](#)]
55. Xu, X.; Si, Z.; Liu, L.; Wang, Z.; Chen, Z.; Ran, R.; He, Y.; Weng, D. CoMoS₂/rGO/C₃N₄ ternary heterojunctions catalysts with high photocatalytic activity and stability for hydrogen evolution under visible light irradiation. *Appl. Surf. Sci.* **2018**, *435*, 1296–1306. [[CrossRef](#)]
56. Jo, W.-K.; Selvam, N.C.S. Z-scheme CdS/g-C₃N₄ composites with RGO as an electron mediator for efficient photocatalytic H₂ production and pollutant degradation. *Chem. Eng. J.* **2017**, *317*, 913–924. [[CrossRef](#)]
57. Rogachev, A.A.; Yarmolenko, M.A.; Rogachou, A.V.; Tapalski, D.V.; Liu, X.; Gorbachev, D.L. Morphology and structure of antibacterial nanocomposite organic–polymer and metal–polymer coatings deposited from active gas phase. *RSC Adv.* **2013**, *3*, 11226–11233. [[CrossRef](#)]
58. Hu, K.; Li, R.; Ye, C.; Wang, A.; Wei, W.; Hu, D.; Qiu, R.; Yan, K. Facile synthesis of Z-scheme composite of TiO₂ nanorod/g-C₃N₄ nanosheet efficient for photocatalytic degradation of ciprofloxacin. *J. Clean. Prod.* **2020**, *253*, 120055. [[CrossRef](#)]
59. Akbari, S.; Moussavi, G.; Giannakis, S. Efficient photocatalytic degradation of ciprofloxacin under UVA-LED, using S,N-doped MgO nanoparticles: Synthesis, parametrization and mechanistic interpretation. *J. Mol. Liq.* **2021**, *324*, 114831. [[CrossRef](#)]
60. Gnanaprakasam, A.; Sivakumar, V.M.; Thirumarimurugan, M. Influencing Parameters in the Photocatalytic Degradation of Organic Effluent via Nanometal Oxide Catalyst: A Review. *Indian J. Mater. Sci.* **2015**, *2015*, 601827. [[CrossRef](#)]